AIP | Physics of Fluids

On the nonlinear development of shear layers in partially vegetated channels

A. C. Lima and N. Izumi

Citation: Physics of Fluids (1994-present) **26**, 084109 (2014); doi: 10.1063/1.4893676
View online: http://dx.doi.org/10.1063/1.4893676
View Table of Contents: http://scitation.aip.org/content/aip/journal/pof2/26/8?ver=pdfcov
Published by the AIP Publishing

PHYSICS OF FLUIDS **26**, 084109 (2014)

On the nonlinear development of shear layers in partially vegetated channels

A. C. Lima[a] and N. Izumi
Graduate School of Engineering, Hokkaido University, 060-8628 Sapporo, Japan

(Received 8 April 2014; accepted 11 August 2014; published online 29 August 2014)

A predictive theory is developed to investigate the nonlinear instability regime of perturbed shear layers in open-channel flows with lateral vegetation. The turbulence is characterized by two distinct scales: a sub-depth turbulence which is associated with the bed shear stress and a large-scale turbulence associated with the large horizontal eddies which develop in the shear layer. The sub-depth turbulence is modeled by assuming a logarithmic vertical distribution of the velocity. Meanwhile, an analogous model for the large-scale turbulence requires the estimation of the transverse velocity profile in the nonlinear state because the growth of the large-scale disturbances expands the shear layer and modifies the velocity distribution across the channel. The nonlinear growth of the disturbances is limited, however, because solid boundaries in the channel play stabilizing mechanisms which lock the amplitude of the large-scale disturbances into a finite-equilibrium state, for which a corresponding transverse velocity profile is determined. A weakly nonlinear stability analysis is performed and the results are validated using experimental data from previous works. © *2014 AIP Publishing LLC*. [http://dx.doi.org/10.1063/1.4893676]

I. INTRODUCTION

Vegetation located at one side of a channel produces velocity inflection and transverse shear, resulting in a Kelvin-Helmholtz instability with large-scale horizontal vortices centered around the edge of the vegetated array. These vortices have a strong influence on the velocity distribution and the amount of discharge conveyed by a channel without overflow, and enhance the lateral exchange of mass and momentum between the vegetated zone and the open channel.

Similar transverse shear flows are observed, for example, in composite channels,[1,2] in inflows at channel junctions,[3,4] or in channels where the bottom roughness varies laterally.[2] The shear layer in the lateral velocity profile has been determined to be the major factor in the generation of instabilities in these transverse shear flows.[1] In addition, the degrees of influence of the bed-friction[2] and gravity[5,6] also play important roles in the stability of these flows. The turbulence due to the bed friction may either enhance or damp the transverse motions. For instance, the transverse shear flow is stabilized if the transverse motions are suppressed by a sufficiently strong bed-friction effect.[2] The gravity effect plays a stabilizing effect on the shear layer, though at large Froude numbers a gravity instability independent of the shear layer is generated.[5,6] The stability characteristics of open channel flows with transverse shear have been studied by means of a linear stability analysis by a number of authors. Some of the major differences among these works can be regarded as the use[1,2,7,8] or not[4–6,9,10] of the inviscid flow assumption, and the use[1,2,4,7–9] or not[5,6,10] of the rigid-lid assumption. Under the inviscid flow assumption, the perturbation equations in these studies are reduced to modified Rayleigh equations, while the formulations with turbulence viscosity lead to modified Orr-Sommerfeld equations. The inviscid flow assumption is a reasonable simplification for flows at large Reynolds numbers or flows where changes in the depth, roughness, or vegetation density across the channel are gradual. The rigid-lid assumption, which does not take the relative

[a]Electronic mail: adriano@eng.hokudai.ac.jp.

importance of gravity into consideration, is a reasonable simplification for small Froude numbers.[5] The linear stability analysis can successfully explain the effects of inertial and gravitational forces, bed shear stress, and shear layer turbulent stress on the stability of transverse shear flows. However, it reflects only the initial state of the growth of infinitesimally small disturbances, while the large-scale vortices correspond to a developed state where nonlinear interactions can no longer be neglected.

The nonlinear interactions may result into an increase in the mixing effect. In order to gain a qualitative understanding of the effect of nonlinear interactions, a nonlinear stability analysis of flow in an open-channel partially covered with vegetation is performed in this study. We employ the St. Venant shallow water equations with the Reynolds stress expressed by a kinematic eddy viscosity representing turbulence with a length scale smaller than the flow depth. This is different from previous models[4,5] where the Reynolds stress is modeled employing a kinematic eddy viscosity which is affected by the lateral motions due to the shear layer.

Although the differential drag between the non-vegetated and vegetated zones excites the instabilities, as the amplitude of the disturbances develops, the solid boundaries of the channel play a stabilizing role in limiting the further growth of the amplitude. Accordingly, the bifurcation pattern determined from the nonlinear stability analysis was typically supercritical, where the amplitude of the perturbations grows to an upper bound derived from the Landau equation. In the case of supercritical bifurcation, the lateral distribution of the velocity and the shear stress at the developed state of the perturbations could be theoretically predicted, allowing the estimation of the kinematic eddy viscosity corresponding to the large-scale turbulences. Experimental data from previous studies support the present theory.

II. GOVERNING EQUATIONS OF FLUID MOTION

In this study, we focus on horizontal vortices generated in the shallow flow in a wide rectangular open channel partially covered with emergent rigid vegetation, as depicted in Figure 1. The vegetation is modeled by an array of regularly spaced cylinders with a uniform diameter installed only on one side of the channel. The model of cylinders as vegetation employed herein has been widely used in previous studies (e.g., Refs. 7, 8, 11–15). The horizontal length scale of the vortices is commonly large compared with the scale of the flow depth. The generation of such thin vortices can be described by the depth-averaged shallow water formulation. The momentum equations in the streamwise and transverse directions ($\tilde{x}$ and $\tilde{y}$) and the continuity equation are

$$\frac{\partial \overline{\tilde{U}}}{\partial \tilde{t}} + \overline{\tilde{U}}\frac{\partial \overline{\tilde{U}}}{\partial \tilde{x}} + \overline{\tilde{V}}\frac{\partial \overline{\tilde{U}}}{\partial \tilde{y}} = \tilde{g}S - \tilde{g}\frac{\partial \overline{\tilde{H}}}{\partial \tilde{x}} - \frac{\overline{\tilde{T}}_{bx} + \overline{\tilde{D}}_x}{\tilde{\rho}\overline{\tilde{H}}} + \frac{1}{\tilde{\rho}}\left(\frac{\partial \overline{\tilde{T}}_{xx}}{\partial \tilde{x}} + \frac{\partial \overline{\tilde{T}}_{xy}}{\partial \tilde{y}}\right), \tag{1a}$$

$$\frac{\partial \overline{\tilde{V}}}{\partial \tilde{t}} + \overline{\tilde{U}}\frac{\partial \overline{\tilde{V}}}{\partial \tilde{x}} + \overline{\tilde{V}}\frac{\partial \overline{\tilde{V}}}{\partial \tilde{y}} = -\tilde{g}\frac{\partial \overline{\tilde{H}}}{\partial \tilde{y}} - \frac{\overline{\tilde{T}}_{by} + \overline{\tilde{D}}_y}{\tilde{\rho}\overline{\tilde{H}}} + \frac{1}{\tilde{\rho}}\left(\frac{\partial \overline{\tilde{T}}_{xy}}{\partial \tilde{x}} + \frac{\partial \overline{\tilde{T}}_{yy}}{\partial \tilde{y}}\right), \tag{1b}$$

$$\frac{\partial \overline{\tilde{H}}}{\partial \tilde{t}} + \frac{\partial \overline{\tilde{U}\tilde{H}}}{\partial \tilde{x}} + \frac{\partial \overline{\tilde{V}\tilde{H}}}{\partial \tilde{y}} = 0, \tag{1c}$$

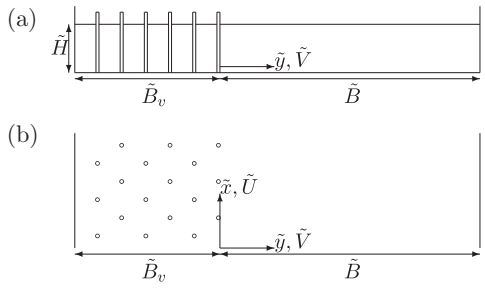

FIG. 1. Conceptual diagram of the channel with vegetation. (a) The cross-sectional view, and (b) the plan view.

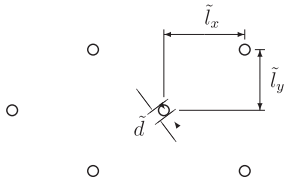

FIG. 2. The plan view of an array of regularly spaced cylinders as a model of vegetation.

where $\tilde{t}$ is time, $\tilde{x}$ is the streamwise coordinate, $\tilde{y}$ is the lateral coordinate, the origin of which is taken at the interface between the vegetated and non-vegetated zones, $\tilde{U}$ and $\tilde{V}$ are the $\tilde{x}$ and $\tilde{y}$ components of the flow velocity, respectively, $\tilde{H}$ is the flow depth, $\tilde{T}_{bx}$ and $\tilde{T}_{by}$ are the $\tilde{x}$ and $\tilde{y}$ components of the bed shear stress, respectively, $\tilde{D}_x$ and $\tilde{D}_y$ are the $\tilde{x}$ and $\tilde{y}$ components of the drag force due to vegetation, respectively, $\tilde{T}_{ij}$ $(i, j = x, y)$ is the Reynolds stress tensor, $\tilde{\rho}$ is the density of water, $\tilde{g}$ is the gravity acceleration, and S is the bed slope of the channel. The tilde denotes dimensional variables and the overline denotes variables averaged over a short time scale corresponding with the sub-depth scale turbulences. The overline is dropped afterwards for simplicity.

The drag force vector $(\tilde{D}_x, \tilde{D}_y)$ is described by the expression

$$(\tilde{D}_x, \tilde{D}_y) = \begin{cases} 0 & \text{in the non-vegetated zone,} \\ \dfrac{\tilde{\rho} C_D \tilde{a} \tilde{H}}{2} (\tilde{U}^2 + \tilde{V}^2)^{1/2} (\tilde{U}, \tilde{V}) & \text{in the vegetated zone,} \end{cases} \tag{2}$$

where C_D is the drag coefficient of vegetation, typically estimated to range from 1 to 2, and $\tilde{a} = \tilde{d}/(2\tilde{l}_x \tilde{l}_y)$ is the parameter which describes the density of vegetation, where $\tilde{d}$ is the diameter of the cylinders and $\tilde{l}_x$ and $\tilde{l}_y$ are the distances between two adjacent cylinders in the $\tilde{x}$ and $\tilde{y}$ directions, respectively, as shown in Figure 2.

The bed shear stress is related to the flow velocity by means of the bed friction coefficient C_f, such that

$$(\tilde{T}_{bx}, \tilde{T}_{by}) = \tilde{\rho} C_f (\tilde{U}^2 + \tilde{V}^2)^{1/2} (\tilde{U}, \tilde{V}). \tag{3}$$

Though the bed friction coefficient C_f is a weak function of the flow depth relative to the roughness height, it is assumed to be constant and common in both the vegetated and non-vegetated zones for simplicity.

With the use of Boussinesq's kinematic eddy viscosity, the depth-averaged Reynolds stresses are expressed by

$$\tilde{T}_{xx} = 2\tilde{\rho} \tilde{\nu}_T \frac{\partial \tilde{U}}{\partial \tilde{x}}, \quad \tilde{T}_{xy} = \tilde{\rho} \tilde{\nu}_T \left(\frac{\partial \tilde{U}}{\partial \tilde{y}} + \frac{\partial \tilde{V}}{\partial \tilde{x}} \right), \quad \tilde{T}_{yy} = 2\tilde{\rho} \tilde{\nu}_T \frac{\partial \tilde{V}}{\partial \tilde{y}}, \tag{4}$$

where $\tilde{\nu}_T$ is the kinematic eddy viscosity. We assume that, in the base state before instability occurs, the flow is already affected by turbulence, the length scale of which is smaller than the flow depth (sub-depth scale turbulence). Where there is no influence of vegetation, the kinematic eddy viscosity $\tilde{\nu}_T$ should correspond to the sub-depth scale turbulence generated by the bottom friction. We employ the logarithmic velocity distribution as a sub-depth scale turbulent velocity distribution due to the bottom friction. The kinematic eddy viscosity then takes a parabolic form, which is depth-averaged from the bottom to the water surface yielding

$$\tilde{\nu}_T = \frac{1}{6} \kappa \tilde{U}_f \tilde{H}_\infty, \tag{5}$$

where $\tilde{U}_f$ $(= \sqrt{\tilde{T}_{bx\infty}/\tilde{\rho}})$ and $\tilde{H}_\infty$ are the friction velocity and the flow depth in the region sufficiently far from the vegetated zone (denoted by the subscript ∞), respectively, and κ is the Kármán constant $(= 0.4)$. We assume that the sub-depth scale turbulence is rather isotropic. Therefore, the above formulation is expected to describe the Reynolds stresses also in the streamwise and lateral directions at a sufficient distance from the vegetated zone.

In the shear layer formed around the boundary between the two zones, and inside the vegetated zone, the velocity and the shear velocity are reduced because of the Reynolds stress and the drag force due to vegetation. In addition, the length scale of sub-depth scale vortices may be affected by a typical length scale of vegetation such as the vegetation spacing. According to the experimental results of Ikeda *et al.*,[11] however, the depth-averaged kinematic eddy viscosity even in the shear layer and the vegetated zone can be represented by (5). This may be attributed to the fact that the sum of the resistant forces (the bed shear stress, the Reynolds stress and the vegetation drag force) remains constant regardless of the reduction in the bed shear stress in the shear layer and the vegetated zone. The kinematic eddy viscosity may be correlated to the total resistant force. Furthermore, since the flow depth and the spacing of vegetation in the experiments carried out by Ikeda *et al.*[11] are both in the same range, the kinematic eddy viscosity in the vegetated zone may not be strongly affected by vegetation. These assumptions and (5) are employed in this study as well.

Fischer *et al.*[16] determined the transverse mixing coefficient $\varepsilon_t \cong 0.15\tilde{U}_f\tilde{H}$ from an approximate average of experimental results in straight rectangular channels from various studies, stating that the above result is likely to be correct for practical purposes in straight rectangular channels with an error bound of ±50%. Based on Fischer *et al.*,[16] Chen and Jirka,[9] followed by Ghidaoui and Kolyshkin[5] and Prooijen and Uijttewaal[4] have assumed values of kinematic eddy viscosity in the range $\tilde{\nu}_t = 0.15$–$0.20\tilde{U}_f\tilde{H}$ for expressing the Reynolds stress corresponding to the small-scale motions. This range of values of kinematic eddy viscosity is, however, affected by the transverse mixing of the shear layer. On the other side, the eddy viscosity in (5) is estimated for the flow before the transverse mixing due to the shear layer occurs. Thus, it assumes a value smaller than $\tilde{\nu}_t = 0.15$–$0.20\tilde{U}_f\tilde{H}$. By employing (5) in the formulation, a base flow consisting of the flow completely undisturbed by the lateral motions due to the development of the shear layer can be derived.

At a sufficient distance from the boundary between the non-vegetated and vegetated zones in the base state normal flow equilibrium condition, $\tilde{U}$ and $\tilde{H}$ are constant, and $\tilde{V}$ vanishes. Thus, (1) allows the solutions

$$\tilde{U}_\infty = \left(\frac{\tilde{g}\tilde{H}_\infty S}{C_f}\right)^{1/2}, \quad \tilde{U}_{-\infty} = \left(\frac{2\tilde{g}\tilde{H}_\infty S}{2C_f + C_D\tilde{a}\tilde{H}_\infty}\right)^{1/2}, \tag{6}$$

where the subscript $-\infty$ denotes the region sufficiently far from the non-vegetated zone. The velocity and flow depth at a sufficient distance from the vegetated zone, $\tilde{U}_\infty$ and $\tilde{H}_\infty$, are used for normalization. The velocities and flow depth are then rendered dimensionless according to the following expressions:

$$(\tilde{U}, \tilde{V}) = \tilde{U}_\infty(U, V), \quad \tilde{H} = \tilde{H}_\infty H. \tag{7}$$

The independent variables $\tilde{x}$, $\tilde{y}$, and $\tilde{t}$ are normalized with the use of the width of the non-vegetated zone $\tilde{B}$, such that

$$(\tilde{x}, \tilde{y}) = \tilde{B}(x, y), \quad \tilde{t} = \frac{\tilde{B}}{\tilde{U}_\infty}t. \tag{8}$$

With the use of the above normalization, the governing equations (1) are rewritten in the form

$$\frac{\partial U}{\partial t} + U\frac{\partial U}{\partial x} + V\frac{\partial U}{\partial y} = -F^{-2}\frac{\partial H}{\partial x} + \beta\left(1 - \frac{T_{bx} + D_x}{H}\right) + \epsilon\left(\frac{\partial^2 U}{\partial x^2} + \frac{\partial^2 U}{\partial y^2}\right), \tag{9a}$$

$$\frac{\partial V}{\partial t} + U\frac{\partial V}{\partial x} + V\frac{\partial V}{\partial y} = -F^{-2}\frac{\partial H}{\partial y} - \beta\frac{T_{by} + D_y}{H} + \epsilon\left(\frac{\partial^2 V}{\partial x^2} + \frac{\partial^2 V}{\partial y^2}\right), \tag{9b}$$

$$\frac{\partial H}{\partial t} + \frac{\partial UH}{\partial x} + \frac{\partial VH}{\partial y} = 0, \tag{9c}$$

where (T_{bx}, T_{by}) and (D_x, D_y) are the normalized bed shear stress and vegetation drag vectors, respectively, written in the form

$$\left(T_{bx}, T_{by}\right) = \left(U^2 + V^2\right)^{1/2} (U, V), \tag{9d}$$

$$\left(D_x, D_y\right) = \begin{cases} \alpha \left(U^2 + V^2\right)^{1/2} H (U, V) & \text{if} \quad -B_v \le y \le 0, \\ 0 & \text{if} \quad 0 \le y \le 1, \end{cases} \tag{9e}$$

where the range $-B_v \le y \le 0$ corresponds to the vegetated zone and the range $0 \le y \le 1$ corresponds to the non-vegetated zone. The above normalized governing equations include the four non-dimensional parameters β, ϵ, F, and α. The parameter β, which expresses the relative importance of the bed shear effect, is dependent on the aspect ratio of the non-vegetated zone $\tilde{B}/\tilde{H}_\infty$, and the bottom friction coefficient C_f, such that

$$\beta = \frac{C_f \tilde{B}}{\tilde{H}_\infty}. \tag{10}$$

The parameter ϵ is associated with the sub-depth kinematic eddy viscosity $\tilde{\nu}_T$, expressed by (5), in the form

$$\epsilon = \frac{\tilde{\nu}_T}{\tilde{U}_\infty \tilde{B}} = \frac{C_f^{1/2} \tilde{H}_\infty}{15 \tilde{B}}. \tag{11}$$

The Froude number F is given by

$$F = \frac{\tilde{U}_\infty}{\sqrt{\tilde{g} \tilde{H}_\infty}} = \left(\frac{S}{C_f}\right)^{1/2}. \tag{12}$$

And the parameter α is related to the vegetation drag and density, and is defined by

$$\alpha = \frac{C_D \tilde{a} \tilde{H}_\infty}{2 C_f}. \tag{13}$$

It is assumed that the channel is sufficiently wide so that a shear layer does not reach the side walls. Under this assumption, it follows that at the side walls, the transverse velocity V vanishes, and the streamwise velocity U asymptotically approaches to constant slip velocities. The following conditions therefore hold:

$$V = 0 \quad \text{at} \quad y = -B_v, 1, \tag{14a}$$

$$\frac{\partial U}{\partial y} = 0 \quad \text{at} \quad y = -B_v, 1. \tag{14b}$$

Right at the boundary between the non-vegetated and vegetated zones, the velocities, flow depth and shear stresses are continuous, such that

$$\lim_{y \to +0} \left(U, V, H, \frac{\partial U}{\partial y}, \frac{\partial V}{\partial y}\right) = \lim_{y \to -0} \left(U, V, H, \frac{\partial U}{\partial y}, \frac{\partial V}{\partial y}\right). \tag{15}$$

The above conditions are valid provided the vegetation is not sufficiently dense for stress jump to take place at $y = 0$. Although there are five matching conditions in (15), if four of them are imposed, the fifth condition is automatically satisfied. Thus, one of these conditions can be dropped afterwards.

III. BASE STATE NORMAL FLOW

The base state flow field is set as the flow undisturbed by the horizontal vortices. The base flow has only a streamwise component. It follows, therefore, that the time and space derivatives and

the transverse velocity vanish and the flow depth is equal to unity under the base state normal flow condition. Equation (9) is then reduced to

$$\beta\left(1-U_0^2\right)+\epsilon\frac{\mathrm{d}^2U_0}{\mathrm{d}y^2}=0 \quad \text{if} \quad 0\le y\le 1, \tag{16a}$$

$$\beta\left[1-U_0^2\left(1+\alpha\right)\right]+\epsilon\frac{\mathrm{d}^2U_0}{\mathrm{d}y^2}=0 \quad \text{if} \quad -B_v\le y\le 0, \tag{16b}$$

where U_0 is the streamwise velocity in the base state, which is a function of only the transverse coordinate y.

The normalization of $(\tilde{U}_\infty, \tilde{U}_{-\infty})$ leads to $(1, \phi)$, where ϕ is the ratio between the undisturbed velocities in the vegetated and non-vegetated zones at a sufficient distance from their boundary, related to the non-dimensional parameter α in the form

$$\phi=\frac{\tilde{U}_{-\infty}}{\tilde{U}_\infty}=\frac{1}{(1+\alpha)^{1/2}}. \tag{17}$$

The domain of ϕ is $0<\phi\le 1$; ϕ approaches to 0 when the vegetation obstructs the flow completely in the vegetated zone ($\alpha\to\infty$), and takes a value of unity when there is no vegetation ($\alpha=0$).

Solving (16) under conditions ((14b)–(15)), we obtain explicit analytical solutions for U_0 in the form

$$U_0(y)=\begin{cases} 3\tanh^2\left[\left(\dfrac{\beta}{2\epsilon}\right)^{1/2}y+\tanh^{-1}\left(\dfrac{\psi+2}{3}\right)^{1/2}\right]-2 & \text{if } 0\le y\le 1,\\[2ex] 3\phi\coth^2\left[-\left(\dfrac{\beta}{2\epsilon\phi}\right)^{1/2}y+\coth^{-1}\left(\dfrac{\psi+2\phi}{3\phi}\right)^{1/2}\right]-2\phi & \text{if } -B_v\le y\le 0, \end{cases} \tag{18}$$

where ψ is the base flow velocity between the non-vegetated and vegetated zones ($y=0$), related with ϕ as

$$\psi=\left(\frac{2\phi^2}{1+\phi}\right)^{1/3}. \tag{19}$$

The streamwise velocity in the base state U_0 is found to be expressed by hyperbolic-tangent and hyperbolic-cotangent functions which are invariant in time and in the streamwise direction and include four non-dimensional parameters, β, ϵ, ψ, and ϕ, where the latter two can be expressed as functions of only α. A sample base state velocity profile is depicted in Figure 3. The velocities at the far right and left correspond to $\tilde{U}_\infty$ and $\tilde{U}_{-\infty}$, respectively, and the value of U_0 at the far left is ϕ.

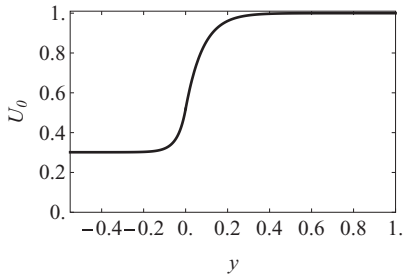

FIG. 3. The lateral distribution of the base flow velocity U_0 for the case $\beta=0.05$, $\epsilon=6\times10^{-4}$, $\alpha=10$.

IV. LINEAR STABILITY ANALYSIS

A temporal linear stability analysis is performed herein. A disturbance undulating in the streamwise direction is introduced to the base state flow. The streamwise and lateral velocities U and V, and the flow depth H are then expanded in the form

$$U(x, y, t) = U_0(y) + AU_1(y)\mathrm{e}^{\mathrm{i}(kx-\omega t)}, \tag{20a}$$

$$V(x, y, t) = AV_1(y)\mathrm{e}^{\mathrm{i}(kx-\omega t)}, \tag{20b}$$

$$H(x, y, t) = 1 + AH_1(y)\mathrm{e}^{\mathrm{i}(kx-\omega t)}, \tag{20c}$$

where A, k, and ω are the amplitude, wavenumber, and angular frequency of the disturbance, respectively. In the scheme of temporal linear stability analysis, k is real while ω is complex such that $\omega = \omega_r + \mathrm{i}\Omega$, where ω_r is the real angular frequency and Ω is the growth rate of the disturbance.

Substituting (20) into the governing equations (9), we obtain the following perturbed equations in the non-vegetated zone:

$$\left[\mathrm{i}(kU_0 - \omega) + k^2\epsilon + 2\beta U_0 - \epsilon\frac{\mathrm{d}^2}{\mathrm{d}y^2}\right]U_1 + \frac{\mathrm{d}U_0}{\mathrm{d}y}V_1 + \left(\mathrm{i}kF^{-2} - \beta U_0^2\right)H_1 = 0, \tag{21a}$$

$$\left[\mathrm{i}(kU_0 - \omega) + k^2\epsilon + \beta U_0 - \epsilon\frac{\mathrm{d}^2}{\mathrm{d}y^2}\right]V_1 + F^{-2}\frac{\mathrm{d}H_1}{\mathrm{d}y} = 0, \tag{21b}$$

$$\mathrm{i}kU_1 + \frac{\mathrm{d}V_1}{\mathrm{d}y} - \mathrm{i}(\omega - kU_0)H_1 = 0, \tag{21c}$$

and the following perturbed equations in the vegetated zone,

$$\left[\mathrm{i}(kU_0 - \omega) + k^2\epsilon + 2\beta U_0(1+\alpha) - \epsilon\frac{\mathrm{d}^2}{\mathrm{d}y^2}\right]U_1 + \frac{\mathrm{d}U_0}{\mathrm{d}y}V_1 + \left(\mathrm{i}kF^{-2} - \beta U_0^2\right)H_1 = 0, \tag{22a}$$

$$\left[\mathrm{i}(kU_0 - \omega) + k^2\epsilon + \beta U_0(1+\alpha) - \epsilon\frac{\mathrm{d}^2}{\mathrm{d}y^2}\right]V_1 + F^{-2}\frac{\mathrm{d}H_1}{\mathrm{d}y} = 0, \tag{22b}$$

$$\mathrm{i}kU_1 + \frac{\mathrm{d}V_1}{\mathrm{d}y} - \mathrm{i}(\omega - kU_0)H_1 = 0. \tag{22c}$$

Since the amplitude of the perturbations A is assumed to be infinitesimally small in the scheme of linear stability analysis, terms containing A^2 were dropped from ((21)–(22)).

A numerical scheme is necessary to solve ((21)–(22)) under the corresponding expanded forms of the boundary and matching conditions ((14)–(15)), as the equations obviously do not admit analytical solutions. We employ a spectral collocation method with the Chebyshev polynomials. In the non-vegetated zone ($0 \le y \le 1$), the variables U_1, V_1, and H_1 are expanded in the form

$$U_1 = \sum_{j=0}^{N} a_j T_j(\xi), \quad V_1 = \sum_{j=0}^{N} a_{(N+1)+j} T_j(\xi), \quad H_1 = \sum_{j=0}^{N} a_{2(N+1)+j} T_j(\xi), \tag{23}$$

and in the vegetated zone ($-B_v \le y \le 0$), they are expanded in the form

$$U_1 = \sum_{j=0}^{N} a_{3(N+1)+j} T_j(\gamma), \quad V_1 = \sum_{j=0}^{N} a_{4(N+1)+j} T_j(\gamma), \quad H_1 = \sum_{j=0}^{N} a_{5(N+1)+j} T_j(\gamma), \tag{24}$$

where a_j ($j = 0, 1, 2, \ldots, 6N+5$) are the coefficients of the Chebyshev polynomials, and $T_j(\xi)$ and $T_j(\gamma)$ are the Chebyshev polynomials in ξ and γ of degree j, respectively. The independent variables ξ and γ both range from -1 to 1, and are related to y by the equations $\xi = 2y - 1$ ($0 \le y \le 1$) and $\gamma = 2y/B_v + 1$ ($-B_v \le y \le 0$), respectively. The expansions (23) and (24) are substituted into the

governing equations (21) and (22), respectively, and the resulting six equations are evaluated at the Gauss-Lobatto points defined by

$$\xi_m = \cos\frac{m\pi}{N}, \quad \gamma_m = \cos\frac{m\pi}{N}, \tag{25}$$

where $m = 0, 1, \ldots, N$. Therefore, the number of points where the governing equations are evaluated is $N+1$. We obtain a system of $6(N+1)$ algebraic equations with $6(N+1)$ unknown coefficients a_0, $a_1, a_2, \ldots, a_{6N+5}$. Eight equations of the system are then replaced by the four boundary conditions (14) and four of the matching conditions (15). The resulting linear algebraic system takes the form

$$\mathcal{M}\begin{bmatrix} a_0 \\ a_1 \\ \vdots \\ a_{6N+5} \end{bmatrix} = 0, \tag{26}$$

where $\mathcal{M}$ is a $6(N+1) \times 6(N+1)$ matrix in which the elements are derived from the coefficients of U_1, V_1, and H_1 in the governing equations (21)–(22) and the boundary and matching conditions (14)–(15). The condition for (26) to have a non-trivial solution is that $\mathcal{M}$ should be singular. Thus,

$$|\mathcal{M}| = 0. \tag{27}$$

The solution of the above equation takes the functional form

$$\omega = \omega(k, \beta, \epsilon, \alpha, B_v, F). \tag{28}$$

There are, therefore, six non-dimensional parameters k, β, ϵ, α, B_v, and F determining the growth rate Ω. We will take, however, the ratio of undisturbed velocities ϕ, which is a function of only α, as the expanded parameter in the nonlinear stability analysis. Though α assumes values from 0 to infinity, ϕ does not range across multiple orders of magnitude. The dependence of the growth rate Ω on k and ϕ is studied in Figure 4. When Ω is positive, the perturbations grow as time progresses, while when Ω is negative, the perturbations decay and vanish. The thick solid line in the figure indicates neutral stability, on which $\Omega = 0$ and the perturbations neither grow nor decay, and divides the plane into stable ($\Omega < 0$) and unstable regions ($\Omega > 0$).

It has been demonstrated (e.g., Refs. 5–7) that Ω as a function of k commonly possesses a characteristic wavenumber k_m associated with the maximum growth rate Ω_m, implying the selection of a preferential wavelength at the linear level. This can be visualized in Figure 4, where Ω is negative in the range of sufficiently small or large values of k, and reaches a maximum value between them.

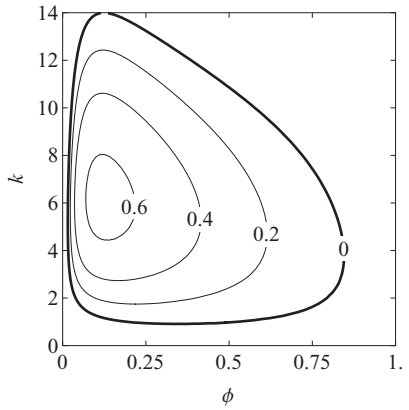

FIG. 4. The contours of the perturbation growth rate Ω in the ϕ–k plane for the case $\beta = 0.05$, $\epsilon = 6 \times 10^{-4}$, $B_v = 0.55$, $F = 0.5$. The thick line indicates the neutral instability ($\Omega = 0$).

Furthermore, according to Figure 4, the flow is stable in the range of large ϕ. As ϕ decreases, Ω increases with a slight increase in k_m, which peaks around the point $(\phi, k) \approx (0.10, 6)$. In the range of $\phi \lessapprox 0.10$, Ω abruptly decreases and k_m slightly decreases with decreasing ϕ. Additionally, Ω becomes negative and the flow becomes stable again when ϕ is close to zero.

In the present analysis, we assume that the kinematic eddy viscosity in the vegetated zone is represented by (5) since the typical length scale of vegetation is not significantly smaller than the flow depth. When the vegetation density is sufficiently large, this assumption may no longer be valid. However, it is natural that the flow becomes stable with decreasing ϕ since the vegetated zone becomes like a cavity region when ϕ is sufficiently small, and the large-scale horizontal vortices are damped by strong retardation effects. Therefore, the contours of Ω in the range of small ϕ in Figure 4 are at least qualitatively correct.

V. WEAKLY NONLINEAR STABILITY ANALYSIS

The neutral state obtained from the linear stability analysis is deviated towards the unstable region as

$$\phi = \phi_c - \zeta^2, \tag{29}$$

where ϕ_c denotes the critical values of ϕ which lie on the neutral instability curve in the ϕ-k plane. According to Figure 4, the instability occurs if $\phi < \phi_c$ with exception of the range of small ϕ. As previously stated, the results in the range of small ϕ might not be quantitatively reliable. Therefore, this range of neutral stability is not considered for expansion in the present analysis and the sign in the expansion of ϕ in (29) is negative.

In the scheme of the present "weakly" nonlinear stability analysis, the time scale of the variation of the amplitude A is much slower than the time scale of the variation of the wavelike part of the disturbance. When ϕ_c is deviated towards the unstable region by the order of ζ^2, the linear growth rate is expected to be of the same order, ζ^2, while the time scale of the variation of A should be of the order[17] (linear growth rate)$^{-1}$, thus ζ^{-2}. The expansion parameter ζ should be small enough to provide that A varies slowly.

We employ a multiple-scale perturbation technique[17] and define the slow time scale t_1 as

$$t = t_0, t_1 = \zeta^2 t. \tag{30}$$

From the above relation, the time derivative becomes

$$\frac{\partial}{\partial t} = \frac{\partial}{\partial t_0} + \zeta^2 \frac{\partial}{\partial t_1}. \tag{31}$$

While the asymptotic expansions in the linear stability analysis (20) are linearized with a small, constant amplitude A, in the nonlinear stability analysis by the growth rate expansion method, the amplitude A varies with the slow time t_1, and the parameter ζ is employed for expansion. The fundamental disturbance is deformed by the nonlinear interactions in the third or higher order of A. We then expand the velocities and flow depth up to this order in the form

$$U(x, y, t) = U_{0,c}(y) + \zeta \hat{U}_1(x, y, t) + \zeta^2 \hat{U}_2(x, y, t) + \zeta^3 \hat{U}_3(x, y, t), \tag{32a}$$

$$V(x, y, t) = \zeta \hat{V}_1(x, y, t) + \zeta^2 \hat{V}_2(x, y, t) + \zeta^3 \hat{V}_3(x, y, t), \tag{32b}$$

$$H(x, y, t) = 1 + \zeta \hat{H}_1(x, y, t) + \zeta^2 \hat{H}_2(x, y, t) + \zeta^3 \hat{H}_3(x, y, t), \tag{32c}$$

where $U_{0,c}$ denotes the base flow velocity for $\phi = \phi_c$.

A. $O(\zeta)$

Substituting (29)–(32) into (9), we obtain the following equations at $O(\zeta)$:

$$G\hat{U}_1 + \frac{\mathrm{d}U_{0,c}}{\mathrm{d}y}\hat{V}_1 + J\hat{H}_1 = 0, \tag{33a}$$

$$K\hat{V}_1 + F^{-2}\frac{\partial \hat{H}_1}{\partial y} = 0, \tag{33b}$$

$$\frac{\partial \hat{U}_1}{\partial x} + \frac{\partial \hat{V}_1}{\partial y} + P\hat{H}_1 = 0, \tag{33c}$$

where the linear operators G, J, K, and P are given by the following expressions:

$$G = \begin{cases} \dfrac{\partial}{\partial t_0} + U_{0,c}\left(2\beta + \dfrac{\partial}{\partial x}\right) - \epsilon\left(\dfrac{\partial^2}{\partial x^2} + \dfrac{\partial^2}{\partial y^2}\right) & \text{if} \quad 0 \le y \le 1, \\ \dfrac{\partial}{\partial t_0} + U_{0,c}\left(2\beta(1+\alpha_c) + \dfrac{\partial}{\partial x}\right) - \epsilon\left(\dfrac{\partial^2}{\partial x^2} + \dfrac{\partial^2}{\partial y^2}\right) & \text{if} \quad -B_v \le y \le 0, \end{cases} \tag{34a}$$

$$J = -\beta U_{0,c}^2 + F^{-2}\frac{\partial}{\partial x}, \tag{34b}$$

$$K = \begin{cases} \dfrac{\partial}{\partial t_0} + U_{0,c}\left(\beta + \dfrac{\partial}{\partial x}\right) - \epsilon\left(\dfrac{\partial^2}{\partial x^2} + \dfrac{\partial^2}{\partial y^2}\right) & \text{if} \quad 0 \le y \le 1, \\ \dfrac{\partial}{\partial t_0} + U_{0,c}\left(\beta(1+\alpha_c) + \dfrac{\partial}{\partial x}\right) - \epsilon\left(\dfrac{\partial^2}{\partial x^2} + \dfrac{\partial^2}{\partial y^2}\right) & \text{if} \quad -B_v \le y \le 0, \end{cases} \tag{34c}$$

$$P = \frac{\partial}{\partial t_0} + U_{0,c}\frac{\partial}{\partial x}, \tag{34d}$$

where α_c is the value of α corresponding to ϕ_c.

The fundamental perturbations at $O(\zeta)$ are assumed to have a similar form to those employed in the linear analysis, such that

$$\hat{U}_1(x, y, t) = A(t_1)U_{11}(y)E + \text{c.c.}, \tag{35a}$$

$$\hat{V}_1(x, y, t) = A(t_1)V_{11}(y)E + \text{c.c.}, \tag{35b}$$

$$\hat{H}_1(x, y, t) = A(t_1)H_{11}(y)E + \text{c.c.}, \tag{35c}$$

where $E = e^{i(k_c x - \omega_c t_0)}$, with k_c and ω_c being the wavenumber and angular frequency corresponding to ϕ_c, respectively, and c.c. being the complex conjugate of the preceding term. Because ω_c is located on the neutral curve, its imaginary part is zero. Substituting the above expansions into (33), we obtain the following equations composed of AE at $O(\zeta)$:

$$G_1 U_{11} + \frac{\mathrm{d}U_{0,c}}{\mathrm{d}y}V_{11} + J_1 H_{11} = 0, \tag{36a}$$

$$K_1 V_{11} + F^{-2}\frac{\mathrm{d}H_{11}}{\mathrm{d}y} = 0, \tag{36b}$$

$$L_1 U_{11} + \frac{\mathrm{d}V_{11}}{\mathrm{d}y} + P_1 H_{11} = 0. \tag{36c}$$

In the above equations, the linear operators G_n, J_n, K_n, L_n, and P_n are given by the following expressions:

$$G_n = \begin{cases} n\mathrm{i}\left(k_c U_{0,c} - \omega_c\right) + 2\beta U_{0,c} + \epsilon(nk_c)^2 - \epsilon\dfrac{\partial^2}{\partial y^2} & \text{if} \quad 0 \le y \le 1, \\ n\mathrm{i}\left(k_c U_{0,c} - \omega_c\right) + 2\beta(1+\alpha_c)U_{0,c} + \epsilon(nk_c)^2 - \epsilon\dfrac{\partial^2}{\partial y^2} & \text{if} \quad -B_v \le y \le 0, \end{cases} \tag{37a}$$

$$J_n = n\mathrm{i}k_c F^{-2} - \beta U_{0,c}^2, \tag{37b}$$

$$K_n = \begin{cases} ni\left(k_c U_{0,c} - \omega_c\right) + \beta U_{0,c} + \epsilon(nk_c)^2 - \epsilon\dfrac{\partial^2}{\partial y^2} & \text{if} \quad 0 \le y \le 1, \\ ni\left(k_c U_{0,c} - \omega_c\right) + \beta(1+\alpha_c) U_{0,c} + \epsilon(nk_c)^2 - \epsilon\dfrac{\partial^2}{\partial y^2} & \text{if} \quad -B_v \le y \le 0, \end{cases} \tag{37c}$$

$$L_n = nik_c, \tag{37d}$$

$$P_n = -ni(\omega_c - k_c U_{0,c}). \tag{37e}$$

Equations (36) are solved by expanding U_{11}, V_{11}, and H_{11} using the Chebyshev polynomials as in ((23)–(24)). The expansions are evaluated at the Gauss-Lobatto points defined by (25) and a system of $6(N+1)$ algebraic equations with $6(N+1)$ unknown coefficients is obtained. Eight equations are then replaced by the four boundary and four of the matching conditions ((14)–(15)) correspondingly expanded. The resulting algebraic linear system takes the following form:

$$\mathcal{M}_{11} \begin{bmatrix} a_{11,0} \\ a_{11,1} \\ \vdots \\ a_{11,6N+5} \end{bmatrix} = 0, \tag{38}$$

where $\mathcal{M}_{11}$ is $\mathcal{M}$ with α, k, and ω replaced by α_c, k_c, and ω_c, respectively, and $a_{11,0}$, $a_{11,1}$, …, $a_{11,6N+5}$ are the unknown coefficients from the expansions using the Chebyshev polynomials. These coefficients are determined from the solution of (38).

B. $O(\zeta^2)$

Substituting (29)–(32) and the solutions at $O(\zeta)$ into (9), we obtain the following equations at $O(\zeta^2)$:

$$G\hat{U}_2 + \frac{\mathrm{d}U_{0,c}}{\mathrm{d}y}\hat{V}_2 + J\hat{H}_2 = A^2E^2I_{22}^{(1)} + \text{c.c.} + AA^*I_{20}^{(1)} + I_{00}, \tag{39a}$$

$$K\hat{V}_2 + F^{-2}\frac{\partial \hat{H}_2}{\partial y} = A^2E^2I_{22}^{(2)} + \text{c.c.} + AA^*I_{20}^{(2)}, \tag{39b}$$

$$\frac{\partial \hat{U}_2}{\partial x} + \frac{\partial \hat{V}_2}{\partial y} + P\hat{H}_2 = A^2E^2I_{22}^{(3)} + \text{c.c.} + AA^*I_{20}^{(3)}, \tag{39c}$$

where the asterisk denotes the complex conjugate of the term itself and $I_{20}^{(j)}$, $I_{22}^{(j)}$ $(j = 1, 2, 3)$ and I_{00} are terms composed of the solutions at $O(1)$ and $O(\zeta)$ and their derivatives. The terms $I_{20}^{(j)}$ and $I_{22}^{(j)}$ $(j = 1, 2, 3)$ are shown in the Appendix, and I_{00} is given by

$$I_{00} = \begin{cases} 0 & \text{if} \quad 0 \le y \le 1, \\ -2\,(1+\alpha_c)^{1/2}\left(\beta + \epsilon\dfrac{\mathrm{d}^2U_{0,c}}{\mathrm{d}y^2}\right) & \text{if} \quad -B_v \le y \le 0. \end{cases} \tag{40a}$$

At $O(\zeta^2)$, the fundamental perturbations are assumed to have the form:

$$\hat{U}_2(x, y, t) = A^2(t_1)U_{22}(y)E^2 + \text{c.c.} + A(t_1)A^*(t_1)U_{20}(y) + U_{00}(y), \tag{41a}$$

$$\hat{V}_2(x, y, t) = A^2(t_1)V_{22}(y)E^2 + \text{c.c.} + A(t_1)A^*(t_1)V_{20}(y), \tag{41b}$$

$$\hat{H}_2(x, y, t) = A^2(t_1)H_{22}(y)E^2 + \text{c.c.} + A(t_1)A^*(t_1)H_{20}(y). \tag{41c}$$

The base flow velocity at $y = -B_v$ is ϕ_c at the neutral state. However, because the actual velocity at $y = -B_v$ is $\phi_c - \zeta^2$, the corrective term $U_{00}(y)$ was introduced in (41a).

Substituting (41) into (39) and dropping terms containing A or A^* yields

$$G_0 U_{00} = I_{00}. \tag{42}$$

Again from the substitution of (41) into (39), we have the following equations composed of terms with A^2E^2:

$$G_2 U_{22} + \frac{\mathrm{d}U_{0,c}}{\mathrm{d}y} V_{22} + J_2 H_{22} = I_{22}^{(1)}, \tag{43a}$$

$$K_2 V_{22} + F^{-2} \frac{\mathrm{d}H_{22}}{\mathrm{d}y} = I_{22}^{(2)}, \tag{43b}$$

$$L_2 U_{22} + \frac{\mathrm{d}V_{22}}{\mathrm{d}y} + P_2 H_{22} = I_{22}^{(3)}, \tag{43c}$$

and the following equations composed of terms with AA^*:

$$G_0 U_{20} + \frac{\mathrm{d}U_{0,c}}{\mathrm{d}y} V_{20} + J_0 H_{20} = I_{20}^{(1)}, \tag{44a}$$

$$K_0 V_{20} + F^{-2} \frac{\mathrm{d}H_{20}}{\mathrm{d}y} = I_{20}^{(2)}, \tag{44b}$$

$$\frac{\mathrm{d}V_{20}}{\mathrm{d}y} = I_{20}^{(3)}. \tag{44c}$$

We solve equations (44b) and (44c) analytically under conditions (14a)–(15), from where we determine V_{20} and H_{20}.

In order to solve (42), (43), and (44a) under the boundary and matching conditions (14)–(15), we expand U_{00}, U_{22}, V_{22}, H_{22}, and U_{20} employing the Chebyshev polynomials as in (23)–(24). By evaluating the corresponding expanded equations and boundary and matching conditions at the Gauss-Lobatto points defined as in (25), we obtain the algebraic systems

$$\mathcal{M}_{00} \begin{bmatrix} a_{00,0} \\ a_{00,1} \\ \vdots \\ a_{00,2N+1} \end{bmatrix} = \begin{bmatrix} f_{00,0} \\ f_{00,1} \\ \vdots \\ f_{00,2N+1} \end{bmatrix}, \tag{45a}$$

$$\mathcal{M}_{22} \begin{bmatrix} a_{22,0} \\ a_{22,1} \\ \vdots \\ a_{22,6N+5} \end{bmatrix} = \begin{bmatrix} f_{22,0} \\ f_{22,1} \\ \vdots \\ f_{22,6N+5} \end{bmatrix}, \tag{45b}$$

$$\mathcal{M}_{00} \begin{bmatrix} a_{20,0} \\ a_{20,1} \\ \vdots \\ a_{20,2N+1} \end{bmatrix} = \begin{bmatrix} f_{20,0} \\ f_{20,1} \\ \vdots \\ f_{20,2N+1} \end{bmatrix}, \tag{45c}$$

where $\mathcal{M}_{00}$ is the $2(N+1) \times 2(N+1)$ matrix of the coefficients of $a_{00,0}, a_{00,1}, \ldots, a_{00,2N+1}$ in the linear system (45a), or $a_{20,0}, a_{20,1}, \ldots, a_{20,2N+1}$ in the linear system (45c), and $\mathcal{M}_{22}$ is the $6(N+1) \times 6(N+1)$ matrix of the coefficients $a_{22,0}, a_{22,1}, \ldots, a_{22,6N+5}$. The terms on the right-side column vectors in (45a)–(45c) correspond to I_{00}, $I_{22}^{(j)}$ ($j = 1, 2, 3$) and $I_{20}^{(1)}$, respectively, or to the right side of the expanded boundary and matching conditions. The unknown coefficients $a_{00,0}, a_{00,1},$

$\ldots, a_{00,\,2N+1}, a_{22,\,0}, a_{22,\,1}, \ldots, a_{22,\,6N+5}$ and $a_{20,\,0}, a_{20,\,1}, \ldots, a_{20,\,2N+1}$ are determined from the solution of the above systems.

C. $O(\zeta^3)$

Substituting (29)–(32) and the solutions at $O(1)$, $O(\zeta)$, and $O(\zeta^2)$ into (9), we obtain the following equations at $O(\zeta^3)$:

$$G\hat{U}_3 + \frac{\mathrm{d}U_{0,c}}{\mathrm{d}y}\hat{V}_3 + J\hat{H}_3 = A^3E^3I_{33}^{(1)} + \text{c.c.} + \left[A^2A^*I_{31}^{(1)} + AI_{31}^{(2)} + \frac{\mathrm{d}A}{\mathrm{d}t_1}I_{31}^{(3)}\right]E + \text{c.c.}, \tag{46a}$$

$$K\hat{V}_3 + F^{-2}\frac{\partial \hat{H}_3}{\partial y} = A^3E^3I_{33}^{(2)} + \text{c.c.} + \left[A^2A^*I_{31}^{(4)} + AI_{31}^{(5)} + \frac{\mathrm{d}A}{\mathrm{d}t_1}I_{31}^{(6)}\right]E + \text{c.c.}, \tag{46b}$$

$$\frac{\partial \hat{U}_3}{\partial x} + \frac{\partial \hat{V}_3}{\partial y} + P\hat{H}_3 = A^3E^3I_{33}^{(3)} + \text{c.c.} + \left[A^2A^*I_{31}^{(7)} + AI_{31}^{(8)} + \frac{\mathrm{d}A}{\mathrm{d}t_1}I_{31}^{(9)}\right]E + \text{c.c.}. \tag{46c}$$

Here $I_{31}^{(i)}$ $(i = 1, \ldots, 9)$ and $I_{33}^{(j)}$ $(j = 1, 2, 3)$ are nonlinear terms composed of the solutions at $O(1)$, $O(\zeta)$, and $O(\zeta^2)$ and their derivatives. At $O(\zeta^3)$, the perturbations are assumed to have the form

$$\hat{U}_3(x, y, t) = A^3(t_1)U_{33}(y)E^3 + \text{c.c.} + U_{31}(y, t_1)E + \text{c.c.}, \tag{47a}$$

$$\hat{V}_3(x, y, t) = A^3(t_1)V_{33}(y)E^3 + \text{c.c.} + V_{31}(y, t_1)E + \text{c.c.}, \tag{47b}$$

$$\hat{H}_3(x, y, t) = A^3(t_1)H_{33}(y)E^3 + \text{c.c.} + H_{31}(y, t_1)E + \text{c.c.}. \tag{47c}$$

Substituting the above expansions into (46), we have the following equations composed of terms containing E (excluding E^3):

$$G_1U_{31} + \frac{\mathrm{d}U_0}{\mathrm{d}y}V_{31} + J_1H_{31} = A^2A^*I_{31}^{(1)} + AI_{31}^{(2)} + \frac{\mathrm{d}A}{\mathrm{d}t_1}I_{31}^{(3)}, \tag{48a}$$

$$K_1V_{31} + F^{-2}\frac{\partial H_{31}}{\partial y} = A^2A^*I_{31}^{(4)} + AI_{31}^{(5)} + \frac{\mathrm{d}A}{\mathrm{d}t_1}I_{31}^{(6)}, \tag{48b}$$

$$L_1U_{31} + \frac{\partial V_{31}}{\partial y} + P_1H_{31} = A^2A^*I_{31}^{(7)} + AI_{31}^{(8)} + \frac{\mathrm{d}A}{\mathrm{d}t_1}I_{31}^{(9)}. \tag{48c}$$

The expansions of U_{31}, V_{31}, and H_{31} employ the Chebyshev polynomials as in (23)–(24), with the difference that the coefficients in the Chebyshev polynomials herein are functions of the amplitude A and its derivative with respect to t_1. The resulting equations are evaluated at the Gauss-Lobatto points as in (25), and a linear system is obtained from (48) with eight equations replaced by the conditions expressed in (14)–(15) such that

$$\mathcal{M}_{11}\begin{bmatrix} a_{31,0}(t_1) \\ a_{31,1}(t_1) \\ \vdots \\ a_{31,6N+5}(t_1) \end{bmatrix} = \begin{bmatrix} f_{31,0}(t_1) \\ f_{31,1}(t_1) \\ \vdots \\ f_{31,6N+5}(t_1) \end{bmatrix}, \tag{49}$$

where $f_{31,\,i}$ $(i = 1, \ldots, 6N + 5)$ are nonhomogeneous terms corresponding to the right-hand side terms of (48) and its corresponding boundary and matching conditions.

Because $\mathcal{M}_{11}$ is a singular matrix, a solvability condition has to be satisfied for (49) to have a solution. This condition is that the determinant of $\mathcal{M}_{11}$ with one of its columns replaced by the

right-hand side column vector should vanish. The resulting linear algebraic system reduces to the Landau equation of the form

$$\frac{dA}{dt_1} = \eta_0 A + \eta_1 |A|^2 A, \tag{50}$$

where η_0 is the linear growth rate of the amplitude and η_1 is the first Landau constant. The Landau constant is sensitively dependent on the normalization of the eigenfunctions at the order $O(\zeta)$. Herein, we employ the condition $U_{11} = 1 + \mathrm{i}$ at $y = 0$.

The signs of the real parts of η_0 and η_1 determine the bifurcation pattern. In the case of $\mathrm{Re}(\eta_0) > 0$ and $\mathrm{Re}(\eta_1) < 0$, we have supercritical bifurcation, where a steady state with an equilibrium amplitude A_e is reached as $t_1 \to \infty$. From (50), we have

$$|A_e| = \sqrt{-\frac{\mathrm{Re}(\eta_0)}{\mathrm{Re}(\eta_1)}}. \tag{51}$$

VI. RESULTS AND DISCUSSION

A. Bifurcation pattern

Table I presents the linear growth rate of the amplitude, η_0, and the first Landau constant, η_1, for the cases $B_v = 0.55$, $F = 0.5$ and varying β and ϵ. In all cases, the expansion expressed in (29) is performed taking the maximum ϕ_c in the ϕ–k plane, which is denoted as $\phi_{c,\,\max}$ hereafter. In the range of typical, moderate values of the parameters β and ϵ, the real part of η_0 is found to be positive and the real part of η_1 is found to be negative, which corresponds to supercritical bifurcation. In the range of large β, the effect of the bottom friction inhibits the effect of the lateral velocity gradient, as has been shown by Chu *et al.*[2] Therefore, the increase in β stabilizes the flow and diminishes the unstable region in the ϕ–k plane and the value of $\phi_{c,\,\max}$. In the range of large ϵ, the dissipation of energy caused by small-scale turbulence suppresses the effect of the transverse mixing. In the range

TABLE I. Parameters on the neutral curve in the ϕ–k plane and the real and imaginary parts of η_0 and η_1 for the case $B_v = 0.55$, $F = 0.5$ and multiple values of β and ϵ.

β	ϵ	$\phi_{c,\,\max}$	k_c	$\mathrm{Re}(\eta_0)$	$\mathrm{Im}(\eta_0)$	$\mathrm{Re}(\eta_1)$	$\mathrm{Im}(\eta_1)$
$10^{-2.0}$	$10^{-4.5}$	0.985	6.48	1.45	3.24	− 7930	− 47.6
$10^{-2.0}$	$10^{-4.0}$	0.973	3.92	0.789	1.95	− 2970	179
$10^{-1.5}$	$10^{-4.5}$	0.974	11.3	2.54	5.66	− 8040	− 126
$10^{-1.5}$	$10^{-4.0}$	0.953	6.50	1.44	3.25	− 2560	− 63.2
$10^{-1.5}$	$10^{-3.5}$	0.913	3.98	0.805	2.04	− 949	− 7.56
$10^{-1.0}$	$10^{-4.5}$	0.950	20.7	4.62	10.4	− 7430	− 226
$10^{-1.0}$	$10^{-4.0}$	0.916	11.5	2.54	5.75	− 2520	− 126
$10^{-1.0}$	$10^{-3.5}$	0.849	6.64	1.41	3.33	− 816	− 74.5
$10^{-1.0}$	$10^{-3.0}$	0.707	4.18	0.785	2.12	− 290	− 41.6
$10^{-1.0}$	$10^{-2.5}$	Stable for any ϕ					
$10^{-0.5}$	$10^{-4.5}$	0.909	36.9	8.04	18.5	− 6960	− 261
$10^{-0.5}$	$10^{-4.0}$	0.839	21.2	4.56	10.6	− 2370	− 216
$10^{-0.5}$	$10^{-3.5}$	0.718	12.1	2.40	6.05	− 780	− 148
$10^{-0.5}$	$10^{-3.0}$	0.343	7.82	0.405	3.74	− 189	− 108
$10^{-0.5}$	$10^{-2.5}$	Stable for any ϕ					
10^{0}	$10^{-4.5}$	0.831	59.1	11.9	28.6	− 5580	357
10^{0}	$10^{-4.0}$	0.713	38.1	7.37	19.1	− 2310	− 362
10^{0}	$10^{-3.5}$	0.352	24.5	1.48	11.7	− 614	− 327
10^{0}	$10^{-3.0}$	Stable for any ϕ					

of very small ϵ, the flow approaches the inviscid case. The unstable region completely disappears for any ϕ if β and ϵ are sufficiently large. For combined small β ($\lessapprox 10^{-2.0}$–$10^{-1.5}$) and large ϵ ($\gtrapprox 10^{-3.5}$–$10^{-3.0}$) the results may not be reliable because the shear layer may be affected by the zero disturbance condition at the walls.

As expressed in (28), although the width of the vegetated zone B_v and the Froude number F also influence the growth rate Ω, these two parameters were kept constant in the results presented in Table I. The growth rate Ω is almost independent of B_v except when B_v is sufficiently small and the displacement of water is suppressed. Concerning F, it has been demonstrated that $\phi_{c,\max}$ does not vary significantly with small and moderate values of F.[10] For large F the flow becomes unstable to gravity and there is no maximum threshold $\phi_{c,\max}$ dividing the ϕ-k plane into a stable and an unstable region.

B. Application to experimental data

The predictive theory developed herein is validated by means of a comparison with results of the laboratory experiments of Ikeda *et al.*[11] and White and Nepf,[8,14] where large-scale horizontal vortices were generated in a channel featuring an array of regularly spaced cylinders installed on one of its sides, which is the same setup assumed in the present analysis. Major hydraulic variables of the experimental runs are listed in Table II. The values of ϕ presented correspond to the ratio of undisturbed velocities observed in the experiments, while $\phi_{c,\max}$ refers to the maximum ϕ on the neutral curve in the ϕ-k plane.

In all experimental runs, the vortices evolved to an equilibrium size and periodicity as the flow developed, indicating the occurrence of supercritical bifurcation. Accordingly, it is predicted that $\mathrm{Re}(\eta_0) > 0$ and $\mathrm{Re}(\eta_1) < 0$ for most cases presented in Table II, with the exception of runs II, III, and XI. These three runs have small β and relatively large ϵ in common, and therefore the analysis may not be applicable, as mentioned in Sec. VI A. In all experiments, however, the channel width exceeds the shear layer and regions of constant velocity are observed outside the shear layer.

1. Mean velocity distribution

The perturbations in the nonlinear state reach a fixed frequency in the experiments. This causes the waves to fall into the reach of a weakly nonlinear description, thus with zero growth rate of

TABLE II. Hydraulic parameters from the experiments of Ikeda *et al.*[11] (runs 1–5) and White and Nepf[8,14] (runs I–XI).

Run	β	$\epsilon(\times 10^{-4})$	F	ϕ	$\phi_{c,\max}$	k_c	$\mathrm{Re}(\eta_0)$	$\mathrm{Re}(\eta_1)$
1	0.061	5.19	0.51	0.303	0.846	4.27	0.880	− 542
2	0.061	5.19	0.77	0.303	0.845	4.27	0.875	− 542
3	0.079	4.48	0.74	0.356	0.838	5.07	1.06	− 593
4	0.164	3.00	0.62	0.462	0.810	8.71	1.82	− 842
5	0.038	6.88	0.48	0.243	0.852	3.16	0.541	− 1040
I	0.058	3.99	0.22	0.124	0.869	4.71	0.982	− 721
II	0.023	4.73	0.21	0.078	0.900	3.05	− 10.8	451
III	0.023	7.31	0.21	0.079	0.861	2.65	0.389	248
IV	0.064	4.02	0.22	0.075	0.862	4.94	1.03	− 705
V	0.061	2.82	0.05	0.079	0.890	5.57	1.19	− 963
VI	0.043	2.86	0.16	0.065	0.905	4.78	1.01	− 998
VII	0.055	3.73	0.21	0.024	0.877	4.76	0.994	− 769
VIII	0.126	4.29	0.08	0.034	0.799	6.54	1.36	− 606
IX	0.089	4.95	0.11	0.033	0.818	5.25	1.08	− 558
X	0.066	5.22	0.34	0.030	0.837	4.50	0.924	− 567
XI	0.032	8.70	0.19	0.018	0.827	2.83	0.169	116

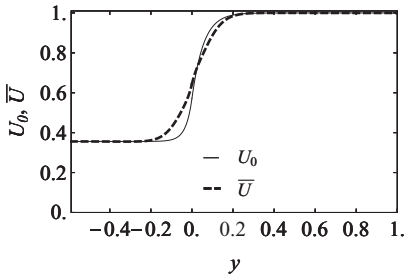

FIG. 5. Transverse profiles of the base state velocity U_0 and mean velocity $\overline{U}$ for run 3 of Ikeda *et al.*[11]

perturbations, and implies that the flow reaches a developed condition for which there is a steady mean velocity. The mean velocity is different from the base flow velocity because of the interaction between the base flow and the disturbance. Under the condition of supercritical bifurcation, it is possible to derive the mean velocity profile corresponding to the fully developed state of perturbations. Figure 5 depicts the base state velocity U_0 and the mean velocity at the equilibrium $\overline{U}$ as functions of the lateral coordinate y, for run 3 of Ikeda *et al.*[11] The overbar denotes the mean at the nonlinear equilibrium state. The mean velocity $\overline{U}$ is equal to $U_{0,c} + \zeta^2(|A_e|^2 U_{20} + U_{00})$, which corresponds to the long time or long x-length average of the streamwise velocity U. The nonlinear development of the perturbations increases the shear layer width, resulting in the milder gradient of $\overline{U}$ visualized in Figure 5. The increase of the shear layer width is mainly at the vegetated zone due to the increase of momentum penetration into this zone. The velocity inflection point is located at $y = 0$ for both U_0 and $\overline{U}$.

Comparisons between the mean velocity transverse profile theoretically determined herein and measurements of Ikeda *et al.*[11] and White and Nepf[14] are presented in Figure 6. The agreement with the experimental runs of Ikeda *et al.*[11] (Figures 6(a)–6(c)) is reasonably good, with the position and magnitude of the velocity gradient along the shear layer well reproduced. Meanwhile the predicted gradient is steeper around the boundary between the non-vegetated and vegetated zones, similar to the experiments.

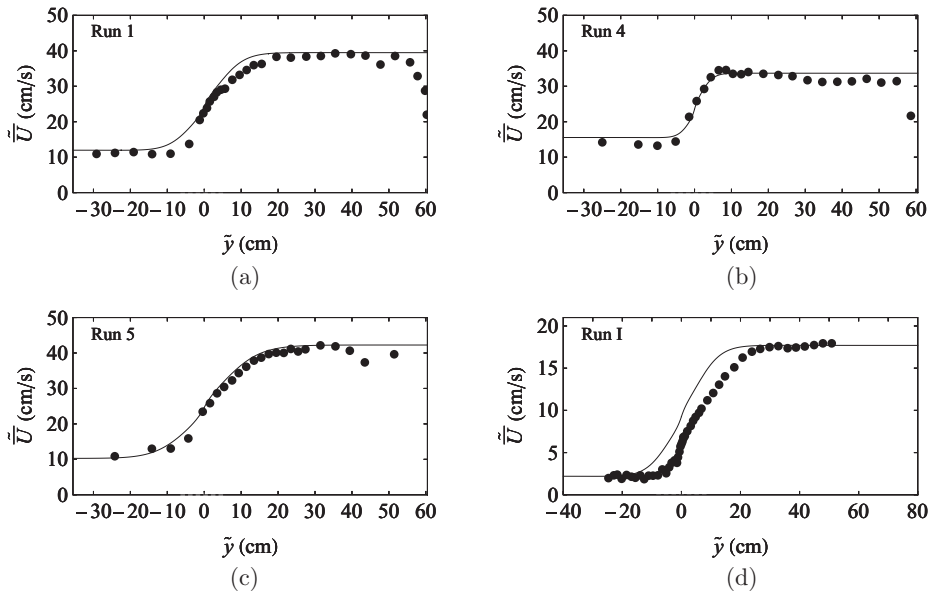

FIG. 6. Lateral distribution of time-averaged velocity for runs 1, 4, and 5 of Ikeda *et al.*[11] and run I of White and Nepf.[14] The solid lines indicate the predictions.

In Figure 6(d), the location of the mixing layer predicted in the analysis is shifted towards the vegetated zone compared to the observed mixing layer. In addition, the predicted gradient is milder in the vegetated zone and steeper in the non-vegetated zone than those in the observed data. This is because the very high density of the vegetated array in Run I suppresses the exchange of momentum between the non-vegetated and vegetated zones. Since we assume that the length scale of the vegetation spacing is not sufficiently smaller than the flow depth, the present model may present discrepancies with the experiments of White and Nepf,[14] where the vegetation density is significantly large, as shown by small values of ratio of undisturbed velocities ϕ of runs I–XI in Table II.

The velocity reduction in the boundary layer at the vicinity of the side walls, clearly visualized in Figures 6(a)–6(b) at the far field in the non-vegetated zone, was not predicted because of the slip condition (14b).

2. Lateral friction velocity

In analogy with the friction velocity corresponding to the bottom shear stress in the far field in the non-vegetated zone defined in Sec. II, a lateral friction velocity can be defined taking the maximum lateral Reynolds stress into consideration, which takes place near the interface between the non-vegetated and vegetated zones ($\tilde{y} = 0$), such that

$$\tilde{U}_{fM}^2 = -\left(\overline{\tilde{U}'\tilde{V}'}\right)_{\max}, \tag{52}$$

where $\tilde{U}'$ and $\tilde{V}'$ are the fluctuations of $\tilde{U}$ and $\tilde{V}$. The negative sign is introduced because $\tilde{U}'$ and $\tilde{V}'$ are anticorrelated around $\tilde{y} = 0$.

Figure 7 presents the profile of $-\overline{\tilde{U}'\tilde{V}'}$ along the transverse direction $\tilde{y}$ for run 3 of Ikeda *et al.*[11] For moderate densities of the array, as in the case depicted in Figure 7, the curve is approximately symmetrical to the vertical axis. As expected, the curve peaks near $\tilde{y} = 0$, where the phase difference between the fluctuating terms $\tilde{U}'$ and $\tilde{V}'$ approaches π rad and the momentum exchange is maximized. Far from $y = 0$, not only the magnitude of the velocity fluctuations decay, but also the phase difference between $\tilde{U}'$ and $\tilde{V}'$ is reduced. In the case of Figure 7, the phase difference reaches $\pi/2$ rad at $\tilde{y} \approx \pm 8$ cm.

In the experiments of White and Nepf,[14] because of the dense arrays, the observed gradient of the transverse distribution of $-\overline{\tilde{U}'\tilde{V}'}$ in the vegetated zone is significantly steeper than in the non-vegetated zone. It follows that the shear layer is mostly located in the non-vegetated zone. The Reynolds stress is maximized 1-2 cm from the array edge in the vegetated zone. Although the transverse distribution of the Reynolds stress of their experiments is not perfectly well reproduced by the present model, the peak value of the distribution could be well estimated. A comparison between observed and predicted friction velocities $\tilde{U}_{fM}$ corresponding to runs I, IV–X[14] is depicted in Figure 8.

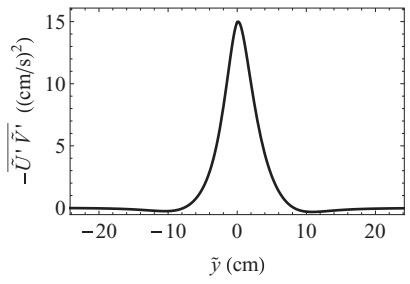

FIG. 7. Predicted distribution of $-\overline{\tilde{U}'\tilde{V}'}$ for run 3 of Ikeda *et al.*[11]

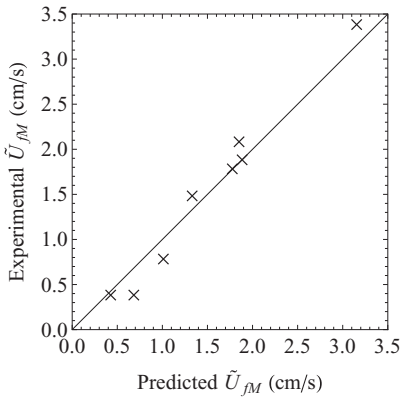

FIG. 8. Comparison between the predicted and measured maximum lateral friction velocity $\tilde{U}_{fM}$, runs I, IV–X of White and Nepf.[14] The continuous line indicates perfect agreement and the × markers correspond to the data.

3. Large-scale kinematic eddy viscosity

The Boussinesq eddy viscosity concept is employed to determine the increased lateral kinematic eddy viscosity at the nonlinear equilibrium state, $\tilde{\nu}_{TM}$, such that

$$-\rho\overline{\tilde{U}'\tilde{V}'} = \rho\tilde{\nu}_{TM}\frac{\mathrm{d}\overline{\tilde{U}}}{\mathrm{d}\tilde{y}}. \tag{53}$$

The sub-depth scale and the large-scale kinematic eddy viscosities, $\tilde{\nu}_T$ and $\tilde{\nu}_{TM}$, respectively, are normalized in the form

$$(\nu_T, \nu_{TM}) = \frac{(\tilde{\nu}_T, \tilde{\nu}_{TM})}{\tilde{U}_f\tilde{H}_\infty}, \tag{54}$$

where $\nu_T = 0.067$ according to (5).

Figure 9 depicts transverse profiles of the large-scale kinematic eddy viscosity ν_{TM} at the region of transverse mixing for the experimental runs of Ikeda *et al.*[11] The continuous lines correspond to ν_{TM} determined from (53) and (54), which hereafter will be denoted as $\nu_{TM}^{(1)}$. The values of $\nu_{TM}^{(1)}$ vary along the transverse direction y and decay far from $y = 0$ as $-\overline{\tilde{U}'\tilde{V}'}$ decays. The bend when $y = 0$ results from the discontinuity of $\mathrm{d}^2\overline{U}/\mathrm{d}y^2$ when $y = 0$. At the shear layer, $\nu_{TM}^{(1)}$ is significantly larger than the undisturbed eddy viscosity ν_T, which is coherent with the assumption that the development of large-scale motions increases the kinematic eddy viscosity. Moreover, $\nu_{TM}^{(1)}$ at the vicinity of the boundary between the two zones ranges from 0.15 to 0.20, which has been employed by Prooijen and Uijttewaal[4,18] and Ghidaoui and Kolyshkin[5] to model the turbulence in mixing layers.

The eddy viscosities determined by Ikeda *et al.*[11] by fitting measurements of their experiments to their proposed averaged velocity solution are denoted by $\nu_{TM}^{(2)}$ and depicted by the dashed lines in Figure 9. For runs 2, 3, and 4, $\nu_{TM}^{(1)}$ and $\nu_{TM}^{(2)}$ agree reasonably well, while, in runs 1 and 5, $\nu_{TM}^{(1)}$ is significantly underestimated compared with $\nu_{TM}^{(2)}$.

Ikeda *et al.*[11] proposed an empirical expression where the kinematic eddy viscosity is a function only of the bottom friction coefficient C_f and the ratio of undisturbed velocities ϕ. This eddy viscosity is denoted as $\nu_{TM}^{(3)}$ and is represented by the dotted lines in Figure 9. Similarly to $\nu_{TM}^{(1)}$, $\nu_{TM}^{(3)}$ is also significantly smaller than $\nu_{TM}^{(2)}$ for runs 1 and 5. Therefore, $\nu_{TM}^{(2)}$ might be overestimated for these runs. Additionally, because F is the only parameter which differs among runs 1 and 2 (see Table II) and this difference is relatively not significant, ν_{TM} for runs 1 and 2 is expected to be similar, contrarily to their corresponding $\nu_{TM}^{(2)}$.

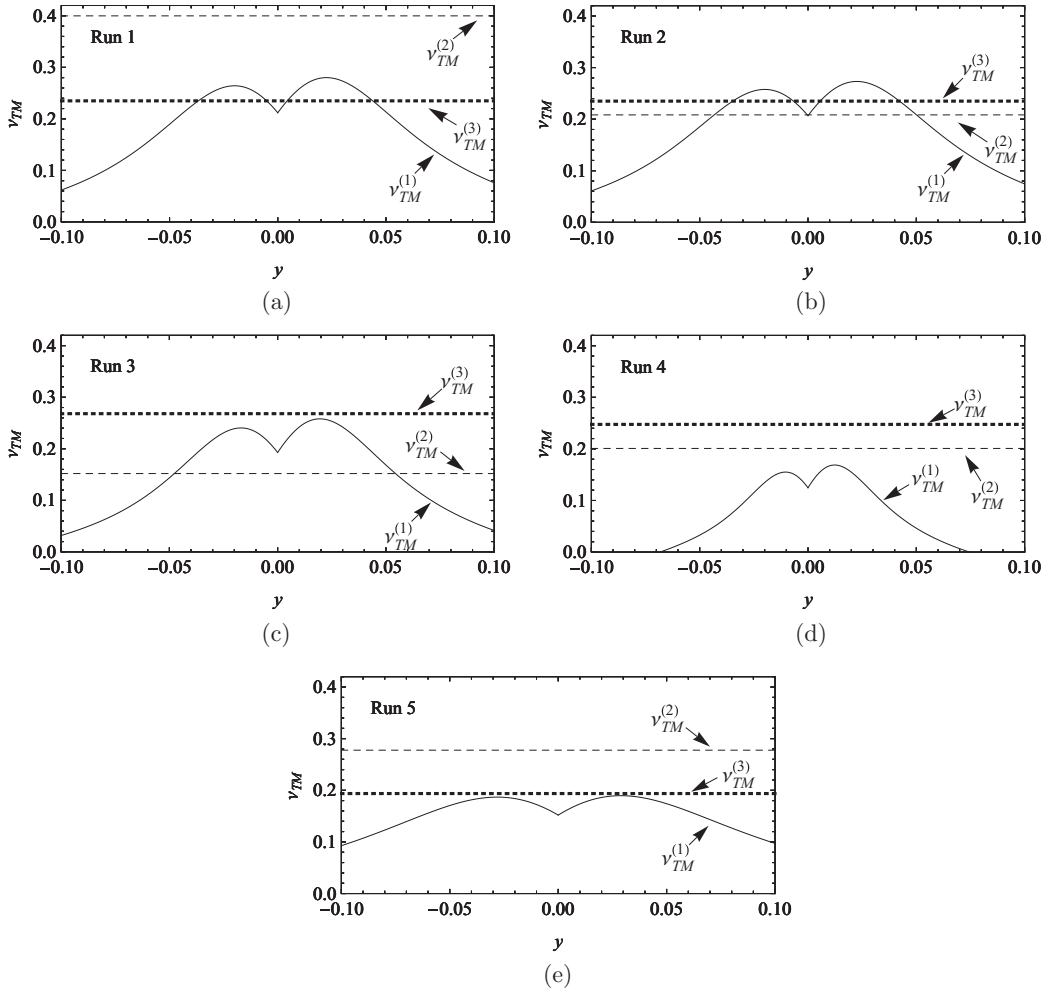

FIG. 9. Large-scale kinematic eddy viscosity at the shear layer for runs 1–5 of Ikeda *et al.*:[11] $\nu_{TM}^{(1)}$: prediction from the present study; $\nu_{TM}^{(2)}$: method described in Ikeda *et al.*[11] where measurements are fitted to a theoretical model; and $\nu_{TM}^{(3)}$: empirical relation from Ikeda *et al.*[11]

4. Periodic fluctuations

Prior to the nonlinear development of the instabilities, when linear mechanisms dominate the transverse mixing in a free shear layer, the Strouhal number for the most amplified wave, $\mathrm{St} = \tilde{f}_m\tilde{\theta}/\tilde{U}_a$, takes the nearly constant value of 0.032 for any hyperbolic tangent base flow profile,[19] where $\tilde{f}_m$ is the natural frequency of the maximum instability, $\tilde{U}_a$ is the average of the far field velocities ($= (\tilde{U}_\infty + \tilde{U}_{-\infty})/2$)), and $\tilde{\theta}$ is the momentum thickness of the undisturbed flow.

In analogy, we determined the Strouhal number based on the frequency for maximum instability obtained from the linear stability analysis, and the momentum thickness of the base-state flow velocity in (18) for the experimental runs listed in Table II. Results were within the range of St from 0.034 to 0.042. Because the development of the perturbations reduce St, the slight overestimation of our results may be because the base flow velocity in (18) is set completely free of the transverse motions of the shear layer, while the hyperbolic-tangent velocity profile for which $\mathrm{St} \approx 0.032$ may have effects of such transverse motions.

As the flow develops and the nonlinear interactions become important, the Strouhal number of the most amplified wave in a free shear layer drops significantly below the neutral value of 0.032.[19] In

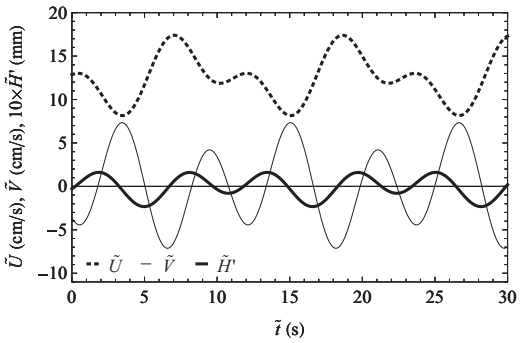

FIG. 10. Calculated time fluctuation of the streamwise and transverse velocities $\tilde{U}$ and $\tilde{V}$ and the flow depth $\tilde{H}$ at $y = -0.6$ cm for run X of White and Nepf.[8]

the partially vegetated channel of the experiments, however, the reduction of the Strouhal number is not so significant. Specifically in the experimental runs of White and Nepf,[8,14] the Strouhal numbers of the dominant frequency at the developed state of perturbations agree with those of the linear results[8] probably because of the high density of the vegetated arrays.

Figure 10 presents the time variation of the velocity components $\tilde{U}$ and $\tilde{V}$ and the flow depth $\tilde{H}$ near the edge of the vegetated array ($\tilde{y} = -0.6$ cm) for run X of White and Nepf.[8] The frequency of the cycle is determined from the Strouhal number of the most amplified wave in the linear state, and the momentum thickness of the developed flow determined herein to be 4.9 cm (the measured value is 4.4 cm). The period of the oscillations is determined herein as 9.14 s, which is close to the observed value of approximately 8.6 s.

VII. CONCLUSIONS

A nonlinear stability analysis of shallow open-channel flow covered with vegetation on one of its sides is performed with the use of the St. Venant shallow water equations. The nonlinear development of the instabilities excited by the velocity difference between the rapid flow in the open channel and the slow flow in the vegetated zone is found to be characterized by supercritical bifurcation in the typical range of the concerning hydraulic parameters, with the exceptions of the small bed friction parameter and the large sub-depth eddy viscosity parameter. The nonlinear analysis is performed by deriving a perturbed state with a slowly varying amplitude.

The Reynolds stress, expressed with the use of Boussinesq's kinematic eddy viscosity, is included in the formulation in order to describe the velocity gradient around the interface between the main channel and the vegetated zone. While previous estimations of the kinematic eddy viscosity in shear layers in parallel shear flows have relied on experiments, herein it is estimated theoretically from the prediction of the velocity fluctuations in the finite-amplitude equilibrium state. The increase of the kinematic eddy viscosity captured by the present model is found to be coherent with the values of kinematic eddy viscosity adopted in formulations of parallel shear flows in previous works.

The distortion of the undisturbed base flow velocity profile by the nonlinear development of the perturbations is predicted, along with the maximum shear stress at the shear layer. Since the rigid-lid assumption is not employed, the model accounts not only for the velocity fluctuations, but also for the fluctuations of the free-surface. The theoretical results are found to be coherent with experimental results from previous studies, though there are discrepancies which can be credited (1) to the limitation of the nonlinear analysis to the vicinity of the neutral curve, (2) to the large vegetation density in some experimental runs, and (3) to the relatively small bed friction parameter and large sub-depth eddy viscosity parameter of some experimental runs, for which the model does not capture the observed steady state of the amplitude development.

APPENDIX: TERMS $I_{20}^{(1)}, I_{20}^{(2)}, I_{20}^{(3)}, I_{22}^{(1)}, I_{22}^{(2)}, I_{22}^{(3)}$

$$I_{20}^{(1)} = \begin{cases} \left(2\beta U_{0,c} U_{11} H_{11}^* - V_{11}^* \dfrac{\mathrm{d}U_{11}}{\mathrm{d}y}\right) + \text{c.c.} - \beta\left(2H_{11}H_{11}^* U_{0,c}^2 + 2U_{11}U_{11}^* + V_{11}V_{11}^*\right) \\ \text{if } 0 \le y \le 1, \\ \dfrac{1}{1+\alpha_c}\left(2\beta U_{0,c} U_{11} H_{11}^* - V_{11}^* \dfrac{\mathrm{d}U_{11}}{\mathrm{d}y}\right) + \text{c.c.} - \beta\left(\dfrac{2H_{11}H_{11}^* U_{0,c}^2}{1+\alpha_c} + 2U_{11}U_{11}^* + V_{11}V_{11}^*\right) \\ \text{if } -B_v \le y \le 0, \end{cases} \tag{A1a}$$

$$I_{20}^{(2)} = \begin{cases} \left(\beta U_{0,c} V_{11} H_{11}^* - V_{11} \dfrac{\mathrm{d}V_{11}^*}{\mathrm{d}y} - \beta U_{11} V_{11}^*\right) + \text{c.c} + \mathrm{i}k_c U_{11} V_{11}^* - \text{c.c.} \\ \text{if } 0 \le y \le 1, \\ \left[\dfrac{1}{1+\alpha_c}\left(\beta U_{0,c} V_{11} H_{11}^* - V_{11} \dfrac{\mathrm{d}V_{11}^*}{\mathrm{d}y}\right) - \beta U_{11} V_{11}^*\right] + \text{c.c} + \dfrac{\mathrm{i}k_c U_{11} V_{11}^*}{1+\alpha_c} - \text{c.c.} \\ \text{if } -B_v \le y \le 0, \end{cases} \tag{A1b}$$

$$I_{20}^{(3)} = -\left[\left(V_{11}\frac{\mathrm{d}H_{11}^*}{\mathrm{d}y} + H_{11}\frac{\mathrm{d}V_{11}^*}{\mathrm{d}y}\right) + \text{c.c.}\right], \tag{A1c}$$

$$I_{22}^{(1)} = \begin{cases} 2\beta U_{0,c} U_{11} H_{11} - V_{11}\dfrac{\mathrm{d}U_{11}}{\mathrm{d}y} - \beta U_{0,c}^2 H_{11}^2 - \mathrm{i}k_c U_{11}^2 - \beta U_{11}^2 - \dfrac{\beta}{2}V_{11}^2 \\ \text{if } 0 \le y \le 1, \\ \dfrac{1}{1+\alpha_c}\left(2\beta U_{0,c} U_{11} H_{11} - V_{11}\dfrac{\mathrm{d}U_{11}}{\mathrm{d}y} - \beta U_{0,c}^2 H_{11}^2 - \mathrm{i}k_c U_{11}^2\right) - \beta U_{11}^2 - \dfrac{\beta}{2}V_{11}^2 \\ \text{if } -B_v \le y \le 0, \end{cases} \tag{A1d}$$

$$I_{22}^{(2)} = \begin{cases} \beta U_{0,c} V_{11} H_{11} - V_{11}\dfrac{\mathrm{d}V_{11}}{\mathrm{d}y} - \mathrm{i}k_c U_{11} V_{11} - \beta U_{11} V_{11} \\ \text{if } 0 \le y \le 1, \\ \dfrac{1}{1+\alpha_c}\left(\beta U_{0,c} V_{11} H_{11} - V_{11}\dfrac{\mathrm{d}V_{11}}{\mathrm{d}y} - \mathrm{i}k_c U_{11} V_{11}\right) - \beta U_{11} V_{11} \\ \text{if } -B_v \le y \le 0, \end{cases} \tag{A1e}$$

$$I_{22}^{(3)} = -2\mathrm{i}k_c U_{11} H_{11} - V_{11}\frac{\mathrm{d}H_{11}}{\mathrm{d}y} - H_{11}\frac{\mathrm{d}V_{11}}{\mathrm{d}y}. \tag{A1f}$$

[1] N. Tamai, T. Asaeda, and H. Ikeda, "Study on generation of periodical large surface eddies in a composite channel flow," Water Resour. Res. **22**(7), 1129–1138, doi:10.1029/WR022i007p01129 (1986).
[2] V. H. Chu, J.-H. Wu, and R. E. Khayat, "Stability of transverse shear flows in shallow open channels," J. Hydraul. Eng. **117**, 1370–1388 (1991).
[3] W. S. J. Uijttewaal and R. Booij, "Effects of shallowness on the development of free-surface mixing layers," Phys. Fluids **12**, 392–402 (2000).
[4] B. C. Prooijen and W. S. J. Uijttewaal, "A linear approach for the evolution of coherent structures in shallow mixing layers," Phys. Fluids **14**, 4105–4114 (2002).

[5] M. S. Ghidaoui and A. A. Kolyshkin, "Linear stability analysis of lateral motions in compound open channel," J. Hydraul. Eng. **125**, 871–880 (1999).
[6] A. A. Kolyshkin and M. S. Ghidaoui, "Gravitational and shear instabilities in compound and composite channels," J. Hydraul. Eng. **128**, 1076–1086 (2002).
[7] S. Ikeda, K. Ohta, and H. Hasegawa, "Instability-induced horizontal vortices in shallow open-channel flows with an inflection point in skewed velocity profile," J. Hydrosci. Hydraul. Eng. **12**, 69–84 (1994).
[8] B. L. White and H. M. Nepf, "Shear instability and coherent structures in shallow flow adjacent to a porous layer," J. Fluid Mech. **593**, 1–32 (2007).
[9] D. Chen and G. H. Jirka, "Absolute and convective instabilities of plane turbulent wakes in a shallow water layer," J. Fluid Mech. **338**, 157–172 (1997).
[10] A. C. Lima and N. Izumi, "Linear stability analysis of open-channel shear flow generated by vegetation," J. Hydraul. Eng. **140**, 231–240 (2014).
[11] S. Ikeda, N. Izumi, and R. Itoh, "Effects of pile dikes on flow retardation and sediment transport," J. Hydraul. Eng. **117**(11), 1459–1478 (1991).
[12] T. Tsujimoto, "Open channel flow with bank vegetation," KHL Commun. **2**, 41–54 (1991).
[13] S. Xiaohui and C. W. Li, "Large eddy simulation of free surface turbulent flow in partially vegetated open channels," Int. J. Numer. Methods Fluids **39**, 919–937 (2002).
[14] B. L. White and H. M. Nepf, "A vortex-based model of velocity and shear stress in a partially vegetated shallow channel," Water Resour. Res. **44**, W01412, doi:10.1029/2006WR005651 (2008).
[15] T. Kitamura, Y. Jia, T. Tsujimoto, and S. Wang, "Sediment transport capacity in channels with vegetation zone," in *Water Resource Engineering '98, Number 326*, edited by S. R. Abt, J. Youngpezeshk, and C. C. Watson (ASCE Publications, Baltimore, 1998).
[16] H. B. Fischer, E. J. List, R. C. J. Koh, J. Imberger, and N. H. Brooks, *Mixing in Inland and Coastal Waters* (Academic, New York, 1979).
[17] J. T. Stuart, "On the nonlinear mechanisms of wave disturbances in stable and unstable parallel flows. part 1. the basic behaviour in plane poiseuille flow," J. Fluid Mech. **9**, 353–370 (1960).
[18] B. C. van Prooijen and W. S. J. Uijttewaal, "On the initiation of large scale turbulence structures in the numerical simulation of shallow mixing layers," in *River Flow 2002 - Proceedings of the International Conference on Fluvial Hydraulics*, edited by D. Bousmar and Y. Zech (Swets & Zeitlinger, Lisse, The Netherlands, 2002).
[19] C.-M. Ho and P. Huerre, "Perturbed free shear layers," Annu. Rev. Fluid Mech. **16**, 365–424 (1984).